Composites Science and Technology 207 (2021) 108732

Contents lists available at ScienceDirect

Composites Science and Technology

journal homepage: http://www.elsevier.com/locate/compscitech

Facile fabrication of lightweight porous FDM-Printed polyethylene/graphene nanocomposites with enhanced interfacial strength for electromagnetic interference shielding

Jingjing Jing [a], Yu Xiong [a], Shaohong Shi [a], Haoran Pei [a], Yinghong Chen [a,*], Philippe Lambin [b]

[a] State Key Laboratory of Polymer Materials Engineering, Polymer Research Institute of Sichuan University, Chengdu, 610065, China
[b] Département de Physique, Université de Namur, 61 Rue de Bruxelles, B-5000, Namur, Belgium

ARTICLE INFO

Keywords:
Fused deposition modeling
Porous structure
Graphene nanoplatelets
Microwave irradiation
EMI shielding

ABSTRACT

In order to shield the massive electromagnetic perturbations and meet the more and more stringent requirement for advanced electronic equipment, development of diverse, lightweight and high-performance electromagnetic interference (EMI) shielding materials is urgent but still challenging. Herein, the facile and green method which combines fused deposition modeling (FDM) 3D printing, ball milling and microwave (MW) irradiation technology was proposed to fabricate exfoliated graphene nanoplatelets (GNPs) incorporated liner low density polyethylene (LLDPE) nanocomposite lightweight parts with porous and complex geometry structure. FDM 3D printing possesses high flexibility for structure design, which can significantly broaden the application of materials in various fields. Benefiting from design of a unique porous lamellar structure, the printed LLDPE/GNPs nanocomposite parts can achieve a prominent EMI shielding effectiveness (SE) of ~32.4 dB (with thickness-normalized specific EMI SE (SSE/t) of 318 dB cm^2/g) in the range of 8.2–12.4 GHz. This remarkable characteristic is due to internal multiple reflections and absorption of electromagnetic (EM) waves. In addition, the specific FDM 3D-printed porous parts prepared by our strategy exhibit a relatively higher EMI SE at a lower density than those lightweight EMI shields in literatures. The use of MW irradiation technology improves mechanical properties, especially for the interfacial bonding strength between filaments. More importantly, this strategy is highly favorable for the fabrication of lightweight porous EMI shields with tailorable and optimized shape/structure, which could be expected to be applied in aerospace fields, portable electronic devices, smart devices and so on.

1. Introduction

With the development of the 5G communication technology based on the gigahertz electromagnetic (EM) waves, the electromagnetic pollution issue, which is caused by the corresponding exponential growth of electronic devices, is receiving more and more attention, not only does it affect the normal functioning and lifetime of the electronic devices but also it threatens the human health [1–4]. Thus, high-efficiency EMI shielding materials are more urgently required to overcome the above challenges than ever [5–8]. As is well known, metal-based shields are the most widely used EMI protectors. However, the metallic shields have some drawbacks such as high density, easy corrosion under air exposure, poor flexibility and relatively inferior processability [9,10]. In addition, they reflect back most of the incident electromagnetic radiations, increasing thereby the EM pollution around them. Meanwhile, nowadays, the development of high-end EMI shielding applications in many fields including wearable clothing devices, portable electronic equipment, aircraft and aerospace facility increasingly relies on light weight, flexibility and environmental stability of material. Therefore, conductive polymer composites (CPCs) are becoming promising candidates to be employed as EMI shields, due to their specific advantages of easy functionalization, facile design, excellent moldability and some other intrinsic properties of the polymer matrix such as lightweight, low-cost and corrosion resistance [11–16]. Obviously, effective reduction of weight, and efficient utilization of energy and materials are crucial to practical EMI shielding applications in various areas [5,17].

In general, lightweight CPCs can be obtained by adopting various preparation methods such as freeze-drying method [18,19],

* Corresponding author.
E-mail address: johnchen@scu.edu.cn (Y. Chen).

https://doi.org/10.1016/j.compscitech.2021.108732
Received 30 September 2020; Received in revised form 2 January 2021; Accepted 15 February 2021
Available online 19 February 2021

compression molding [20–22] and foaming process [23,24]. In these processes, however, the conductive network distributed in the polymer matrix is hard to be controlled with the possible consequence of lowering the effective conductivity [12,25]. For instance, lightweight PEI/CNT foams prepared via a sinter molding and further supercritical CO_2 ($scCO_2$) foaming, demonstrate an EMI shielding efficiency (SE) ranging from 35.3 dB to 5.5 dB with decreasing density from 1.27 to 0.61 g/cm^3 [23]. However, it is found that the EMI shields with low density are far from meeting the requirements of commercial applications. In addition, the aforementioned technologies are also facing great challenges in fabricating architectures with complex geometric structure. This would surely restrict their applications in some special fields. More recently, the 3D printing technology, also known as additive manufacturing (AM), has attracted more and more attention. Among the 3D printing technologies, fused deposition modeling (FDM) is currently one of the most frequently applied technologies in practice [26–29]. FDM 3D printing involves a filament-based printing process, during which the filament is first fed into a heating nozzle, melted and then extruded out of the nozzle. Finally, the extruded melts are deposited onto a build plate to generate a three-dimensional structure in a layer-by-layer process [30]. Due to the high designing and manufacturing flexibility [31–33] of FDM 3D printing technology, it has been receiving more and more attention and applied to fabricate the EMI shields for lightweight and diversity purposes [34–36]. However, up to now, less work has been involved in preparing the lightweight porous EMI shields through FDM 3D printing strategy and investigating the effects of the printing structure on the EMI SE. Furthermore, it is worth noting that good-quality interfaces can induce beneficial multiple reflections of the EM wave in the interior of the 3D printed part [37].

However, the poor interlaminar bonding strength still remains a challenge for the 3D printed parts. In order to address this issue, specific heat treatments has been reported in several studies [38,39]. As we know, in the conventional heating mode, a material is generally heated from outside to inside through radiation, conduction and convection [22,40]. However, this way of doing would require much heating time and the heating efficiency is also relatively low, especially for parts with large size and complicated structure, thus easily forming unevenly distributed heating flow and leading to local overheating. Furthermore, some thermal-sensitive particles are incorporated into the 3D-printed parts for further thermal treatment, but there could be low efficiency and complicated treatment process to some extent. For instance, a conventional heat treatment technology has been applied to reduce the voids between deposition filaments in the FDM 3D printed Polywax parts incorporated with thermally expandable microspheres [38]. However, for the FDM 3D printed parts without thermally expandable microspheres incorporated, the heating efficiency was very low and the enhancement of the mechanical performance (particularly the compressive strength) was obviously limited, even if the heating time was extended or the heating temperature was increased. Obviously, the resulting thermally treated structures should affect the performance enhancement of the CPCs parts, and incorporating these microspheres also would complicate the preparation process. Recently, a microwave (MW) sintering strategy has been developed in our research group to fabricate CPCs with excellent EMI SE [21–23]. As is well known, MW irradiation may involve electromagnetic radiations with variable frequencies from 300 MHz to 300 GHz. When the MW radiation energies are absorbed by non-metallic materials, they can be transformed into heat through the interaction of the radiations with the material molecules. Clearly, this is a volumetric heating process which is efficient, energy saving, clean and environmentally friendly [22]. Compared with the conventional heating technology, MW heating strategy demonstrates an improved heating uniformity, shorter heating time and the higher efficiency [39]. In addition, more importantly, the MW irradiation possesses selective heating feature for different materials, which mainly depends on their electromagnetic characteristics. Generally, thermoplastic polymers are transparent to MW, while conductive fillers, especially for carbon nanotubes (CNTs) and graphene nanoplatelets (GNPs), are excellent MW absorbents and can be heated vigorously upon MW irradiation [41].

In the present work, a facile strategy which combines ball milling, FDM 3D printing, and microwave (MW) irradiation was proposed to prepare the lightweight porous CPCs. Graphene nanoplatelets were carefully selected as both the conductive filler and MW absorbent to fabricate the FDM printed CPCs with enhanced interlaminar bonding strength. Linear low-density polyethylene (LLDPE) was employed as polymer matrix due to its lightweight, low-cost and excellent processability. Further, the ball-milling technology was adopted to exfoliate and selectively distribute the GNPs onto the surface of LLDPE particles to obtain GNPs coated LLDPE powders due to strong impact and shear forces of colliding balls. Then, FDM printing and MW irradiation strategy were effectively combined to prepare the LLDPE/GNPs nanocomposite parts with porous and complex geometry. The results show that the fabricated LLDPE/GNPs composite parts with tailorable density and structure/shape exhibit excellent EMI SE, outstanding specific EMI SE (SSE/t) and significantly enhanced interfacial bonding strength. The FDM printed LLDPE/GNPs parts would accordingly show great potential of applications and promising prospects as candidates in aerospace systems, portable electronic devices and smart devices.

2. Experimental section

2.1. Materials

Thermoplastic linear low-density polyethylene (LLDPE, 2720A) particles with a size distribution of 100–200 μm, a density of 0.92 g/cm^3, a melting temperature of 125 °C, and a melt index about 20 g/10min were provided by Sinopec Maoming Petrochemical Co., Ltd., China. Graphene nanoplatelets (GNPs,SE1233) with a surface area of 400–550 m^2/g were obtained from The Sixth Element (Changzhou) Materials Technology Co., Ltd., China.

2.2. Preparation of LLDPE/GNPs filaments

A schematic presentation of the fabrication of LLDPE/GNPs nanocomposites and FDM 3D printing process is illustrated in Fig. 1. To prepare the GNPs coated LLDPE composite powders, LLDPE powder was first mixed with various loading of GNPs (1, 2, 4, 6, 8 and 10 wt%) using a ball milling machine (QM-3SP4, Nanjingnanda instrument Co., Ltd, China) at 350 rpm for 1 h. The prepared composite powders were then extruded in a single-screw extruder (RM-200C, Harbin HAPRO Electric Technology Co., Ltd. China) to prepare the corresponding filaments through careful control of the extrusion temperature at 170 °C, screw rotation speed adjusted at 15 rpm and diameter of the extruded filaments set at 1.75 ± 0.05 mm (by adjusting the drawing speed). Here below, the LLDPE/GNPs filaments with different content of GNPs are named LLDPE/1 GNPs, LLDPE/2 GNPs, LLDPE/4 GNPs, LLDPE/6 GNPs, LLDPE/8 GNPs and LLDPE/10 GNPs, respectively, where the "LLDPE/nGNPs" means that n wt% loading of GNPs were incorporated in LLDPE matrix.

2.3. Fabrication of LLDPE/GNPs nanocomposite parts via FDM 3D printing

All the measured samples were fabricated on a German RepRap × 350pro FDM printer. The corresponding 3D model was constructed using Pro/Engineer 5.0, and then exported as a STL file for printing. The following 3D printing parameters were adopted: nozzle diameter of 0.4 mm, layer thickness of 300 μm, nozzle temperature of 170 °C and printing speed of 150 mm/min. To investigate the influence of different printing structure on the EMI SE of the obtained LLDPE/GNPs nanocomposite parts with cylindrical shape, three different filling patterns were selected: 0 × 0 (pattern 1), 0 × 60 (pattern 2) and −60 × 0 × 60

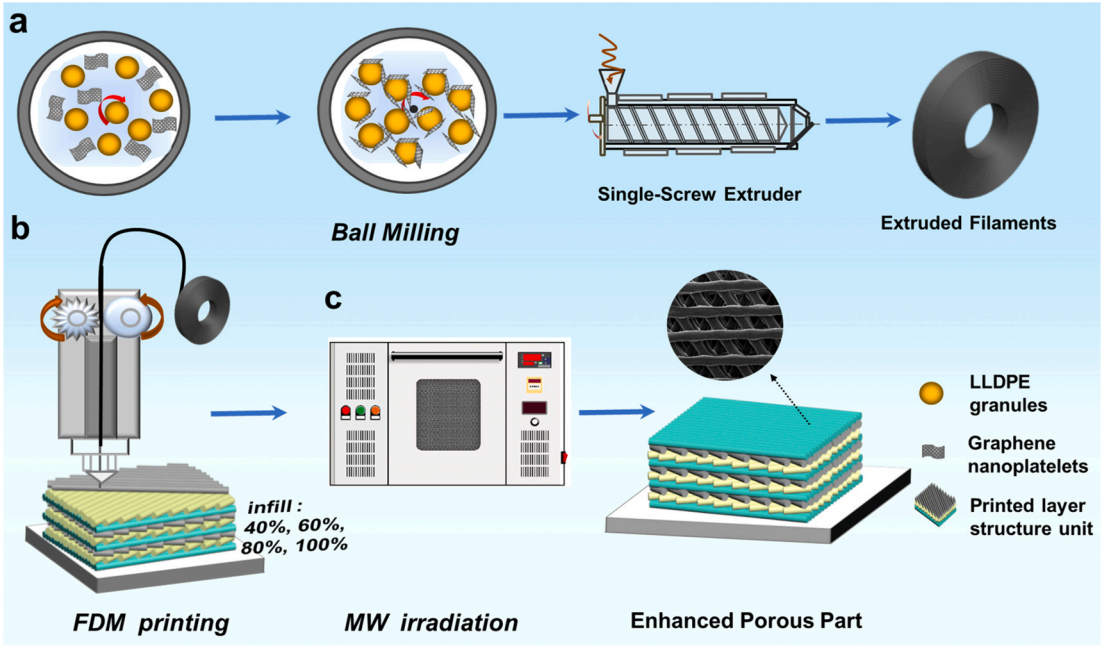

Fig. 1. Schematic diagram for the preparation of LLDPE/GNPs nanocomposite filaments (a), FDM 3D printing process (b) and MW irradiation post-manufacture process (c).

(pattern 3). These filling patterns are illustrated in Fig. S1. The notations 0 × 0, 0 × 60 and −60 × 0 × 60 mean that the printed filaments were alternately deposited onto the building plate along 0°, 0°/60° and −60°/0°/60° directions (relative to a fixed horizontal direction), respectively. In addition, the object infill density was chosen at 40, 60, 80 and 100%, respectively. When the infill density is less than 100%, it is believed that the 3D printed part possesses a porous structure. For convenient discussion, the obtained LLDPE/GNPs nanocomposite parts with different printing pattern and infill density are named $LG_{m\text{-}n}$, where the "$LG_{m\text{-}n}$" means that the samples were fabricated using printing pattern "m" and infill density of "n%", respectively. For instance, LG_1, LG_2 and LG_3 samples represent the LLDPE/GNPs parts printed with pattern 1, 2 and 3, respectively; $LG_{1\text{-}40}$ sample represents the LLDPE/GNPs nanocomposite parts which were obtained by adopting printing pattern 1 and infill density of 40%. However, for tensile test, the required dumbbell-shaped samples (with dimension of length 25 mm, width 5 mm (narrow section) and 10 mm (wide section), and thickness 2 mm) were printed according to three different filling patterns (0 × 0, 45 × 45 and 90 × 90). The corresponding printed samples were named FS_0, FS_{45} and FS_{90}, respectively, as illustrated in Fig. S2. Here again 0 × 0, 45 × 45 and 90 × 90 mean that the printing filaments are deposited onto the building plate along 0°, 45° and 90° direction (relative to sample length direction), respectively. To investigate the effect of the MW irradiation on the mechanical property and EMI SE, the corresponding FDM parts were put in a microwave furnace for irradiation sintering. Considering that a large concentration of GNPs in LLDPE would lead to strong MW absorption and a high temperature, we specially sintered the LLDPE/GNPs 3D printed parts with different loading of GNPs (0–10.0 wt%) over different irradiation time (10–40 s) under a fixed MW power of 300 W because long irradiation time and high irradiation power could destroy the sample. The irradiation time for the sample with 0.0/2.0, 4.0, 6.0 and 8.0/10.0 wt% loading of GNPs was selected as 40, 30, 20 and 10 s, respectively. The MW irradiated sample was correspondingly named M-FS_x where x represents one of the 3 filling patterns (0 × 0, 45 × 45 and 90 × 90). The temperature distribution of LLDPE/GNPs nanocomposites at different irradiation time and different GNPs loading was provided in Supplementary Information (Fig. S3). As can be seen, LLDPE/6 GNPs and LLDPE/10 GNPs can reach up to 140 °C for irradiation (300 W) about 20s and 10s, respectively.

2.4. Characterization

The morphology of the surface and the fractured surface of the filaments and the corresponding 3D printed parts was investigated with a scanning electron microscope (SEM) (FEI Instrument, USA) at an accelerating voltage of 20 kV. The tensile properties of LLDPE/GNPs 3D printed parts (FS_0, FS_{45} and FS_{90}) were evaluated using an Instron 5567 instrument (Instron Co., Ltd, United States) and the crosshead speed was 20 mm/min. The bulk densities (ρ) of the sintered 3D printed parts were obtained from the equation ρ = m/v, where m and v are the weight (g) and volume (cm^3) that were measured with an electronic balance and a vernier caliper, respectively. Rheological measurements of the LLDPE/GNPs nanocomposites were carried out on a parallel-plate rotational rheometer (TA Instruments, USA). Dynamic frequency sweeps were carried out by using a 25 mm diameter parallel plate with a 2 mm sample thickness and a fixed strain of 5% at 170 °C. The scanning frequency ranged from 0.01 to 100 Hz. The EMI SE performance was evaluated by using a coaxial test cell (APC-7 connector) in conjunction with an Agilent N5230 vector network analyzer (USA) from 8.2 to 12.4 GHz. FDM printed disk samples with 13.0 mm diameter and 2 mm thickness were completely enclosed by the coaxial test cell consisting of two waveguide connectors and the S-parameters (S_{11} and S_{21}) were accordingly obtained [33]. The corresponding electromagnetic reflection shielding (SE_R), absorption shielding (SE_A) and total EMI SE (SE_T) were calculated from the measured scattering parameters (S_{11} and S_{21}) according to the following equations [24,42].

$$R = {S_{11}}^2 = {S_{22}}^2,\ T = {S_{12}}^2 = {S_{21}}^2 \tag{1}$$

$$SE_R = 10lg\left(\frac{1}{1-R}\right) = 10lg\left(\frac{1}{1-{S_{11}}^2}\right) \tag{2}$$

$$SE_A = 10lg\left(\frac{1-R}{T}\right) = 10lg\left(\frac{1-{S_{11}}^2}{{S_{21}}^2}\right) \tag{3}$$

$$SE_T = SE_R + SE_A = 20lg(S_{21}) \tag{4}$$

3. Results and discussion

3.1. Preparation and characterization of LLDPE/GNPs nanocomposite filaments

The GNPs coated LLDPE particles prepared by ball-milling and the corresponding characterizations are illustrated in Supplementary Information (Fig. S4). From the magnified SEM image of the coated particles, it can be seen that the surface of dark modified LLDPE particles is obviously rough. There are many GNPs particles uniformly and tightly attached to the surface of LLDPE particles under the effect of the very strong impact and shear force of the grinding balls generated during ball milling. The occurrence of the obvious XRD featured diffraction peak of GNPs in LLDPE/6 GNPs composite proves the existence of GNPs there. To investigate the influence of ball milling on the exfoliation of GNPs particles, Raman spectroscopy measurement was applied to characterize the exfoliation of GNPs produced by ball milling. The results are shown in Fig. 2. As can be seen, the intensity of G′-band at approximately 2680 cm^{-1} increases relative to the small peak nearby with increasing milling time from 0 to 60 min (Fig. 2a). It is simultaneously noted that the ball milling also causes a red shift of the G′-band. The above results suggest that the ball milling process could decrease the thickness of GNPs layers, which is consistent with a previous work reported by other researchers [43]. Furthermore, it is known that the G-band is associated with the in-plane vibration of the SP^2 carbon atom of GNPs [33]. When the number of GNPs layers decreases, the intensity of the G-band decreases significantly, and meanwhile the intensity of G′-band increases instead [43]. From Fig. 2a, it can be also seen that, with extension of the ball milling time, the intensity I_G of G-band located at 1585 cm^{-1} shows the obviously decreasing tendency, while the intensity $I_{G'}$ of G′-band located at 2680 cm^{-1} exhibits the significantly increasing tendency. As a result, the $I_G/I_{G'}$ (the intensity ratio of G-band to G′-band) value of the milled GNPs is significantly lower than that of the unmilled GNPs. The significant decrease in $I_G/I_{G'}$ ratio with time indicates the successful exfoliation of GNPs under the effect of ball milling. To further investigate and confirm this observation, TEM and AFM characterizations of the samples were carried out as well. Compared with TEM image of the pristine GNPs (Fig. 2b_i), the one of milled GNPs (Fig. 2b_{ii}) shows a typical few-layer graphene which was exfoliated by ball milling for 60 min, where the GNPs platelets present a micro-scale length and a much thinner thickness. The AFM results of Fig. 2c also show that the GNPs extracted from the coated LLDPE particles after 60 min treatment possess an obviously decreased thickness of 3.5 nm. In combination with the previous Raman analyses data, it can be concluded that the ball-milling technology can really lead to the exfoliation of GNPs.

On the basis of successful GNPs exfoliation by ball milling, the milled mixture of LLDPE and GNPs were extruded to prepare nanocomposite filaments. The digital photos of the obtained filaments of pure LLDPE and nanocomposites (with 6 and 10 wt% GNPs incorporated) are shown in Fig. S5. As can be seen, the appearance of the latter is as smooth as that of the former. The morphology of the fractured filaments surface is illustrated in Fig. 2d and e. It can be seen that pure LLDPE filaments shows a relatively flat fractured surface (Fig. 2$d_{i\text{-}ii}$). After ball milling process, the LLDPE/10 GNPs nanocomposite filaments show no obvious agglomeration of GNPs particles and the well-dispersed GNPs network structures existing in LLDPE matrix (Fig. 2e_i&2e_{ii}). This is because under the effect of the single-screw extrusion shear force field, the segregated GNPs network structure in the coated polymer particles could be dynamically stretched to form an interconnected network [44,45]. The related formation mechanism is further illustrated in Fig. S6 (Supplementary Information). The above results indicate that the ball milling process contributes to the exfoliation of GNPs particles and may lead to the formation of connected network structures.

3.2. FDM 3D printing of LLDPE/GNPs nanocomposites

To further evaluate the 3D printability of the LLDPE/GNPs nanocomposites, the apparent viscosity (η) and storage modulus (G′) dependence on frequency (ω) is shown in Fig. 3a and b. It can be seen that the incorporation of rigid GNPs particles in LLDPE matrix significantly increases both η (Fig. 3a) and G′ (Fig. 3b). This increase can be attributed to enhanced interfacial interactions between GNPs and LLDPE molecular chains due to the high surface area of the exfoliated GNPs and the formation of GNPs networks in polymer matrix [46,47]. In addition, the pronounced G′ plateau of the nanocomposites with 6–10 wt% loading of GNPs occurs at low frequency and this adequately indicates the formation of a well-interconnected filler networks structure in nanocomposites [45,48]. Furthermore, it is also found that the apparent

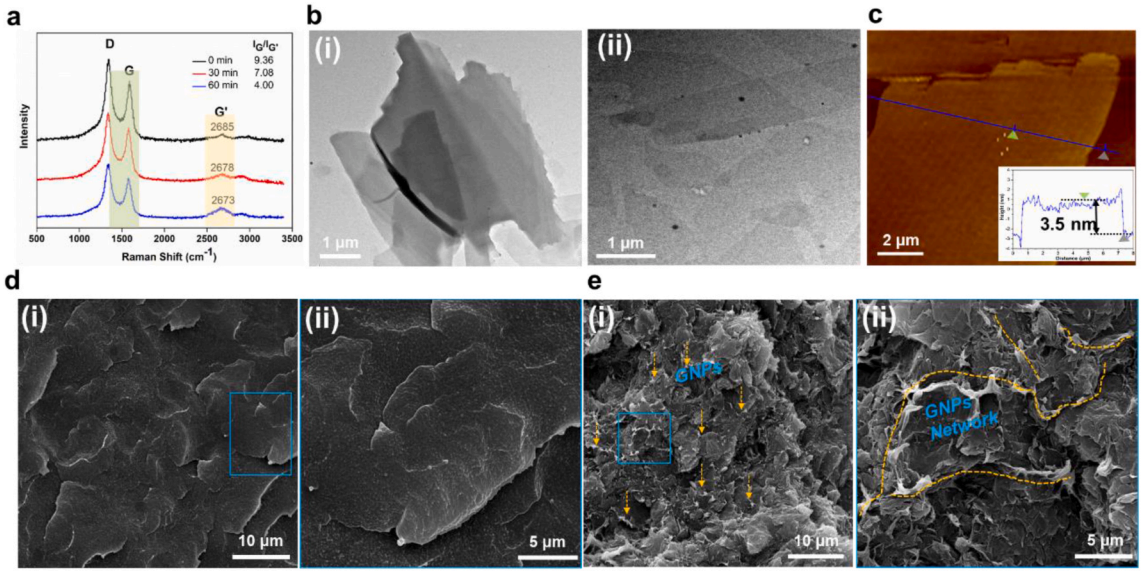

Fig. 2. Preparation and morphology of LLDPE/GNPs composites filaments. Raman spectra of LLDPE/10 GNPs co-powders with different milling time at 532-nm excitation wavelength (a), TEM image of pristine GNPs particles (b_i) and GNPs platelets separated from co-powders (b_{ii}), AFM image of GNPs deposited on mica using ethanol solution (c) (inset is the corresponding height curve), and SEM images of the fractured surface of as-prepared filaments, pure LLDPE ($d_{i\text{-}ii}$) and LLDPE/10 GNPs ($e_{i\text{-}ii}$).

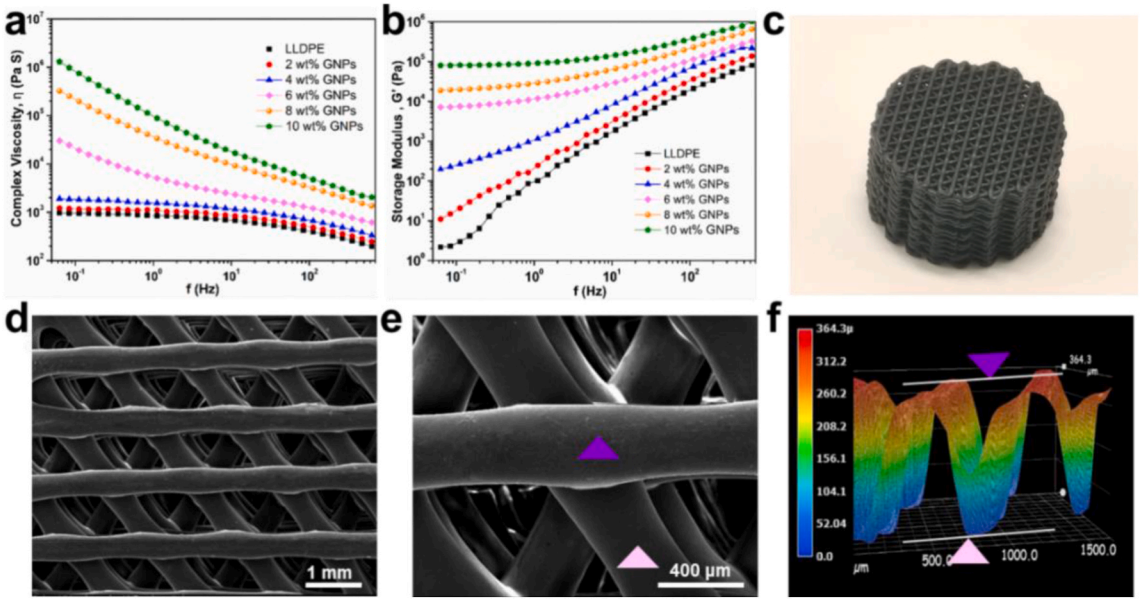

Fig. 3. Printability exploration of LLDPE/GNPs nanocomposites. Dynamic rheological properties: complex viscosity η (a) and storage modulus G′ (b) of pure LLDPE and LLDPE/GNPs nanocomposites with different GNPs loading versus angular frequency at 170 °C; FDM 3D-printed porous part of LLDPE/10 GNPs with 40% infill density: digital photo (c), SEM image of the internal microstructure in low magnification (d) and high magnification (e); super-depth-of-field image of the corresponding FDM 3D-printed part along thickness direction (f).

viscosities (η) of all samples almost linearly decrease with increasing frequency, suggesting that the LLDPE/GNPs nanocomposites have an obvious shear thinning behavior. This property could ensure that the melt of filament can smoothly pass through the nozzle and the corresponding parts could be successfully printed. Fig. 3c–e shows the digital photo of a printed cylindrical part of LLDPE/10 GNPs together with SEM images of its porous microstructure. It can be clearly seen that the printed part exhibits a perfect profile (Fig. 3c), and the deposited filaments are aligned regularly and also present a very smooth surface. Each printed layer of the parts has the same thickness. More importantly, triangle porous structures consisting of multilayer filaments are formed through the FDM 3D printing. It is worth noting that such the porous structures inside the printed parts could effectively enhance the interfacial areas, which are advantageous for the attenuation of the electromagnetic waves, thus enhancing the EMI shielding property (this will be discussed below). The formation of the bamboo joint-like morphology is caused by the deformation of melt of the new filaments deposited onto the old ones upon bonding. This could happen only when there is an angle between the two adjacent layers of the deposited filaments with an infill density less than 100%. Additionally, the super-depth-of-field images of 3D printed parts (Fig. 3f) clearly show the layer thickness of the printing filaments could be as small as the designated 300 μm, indicating

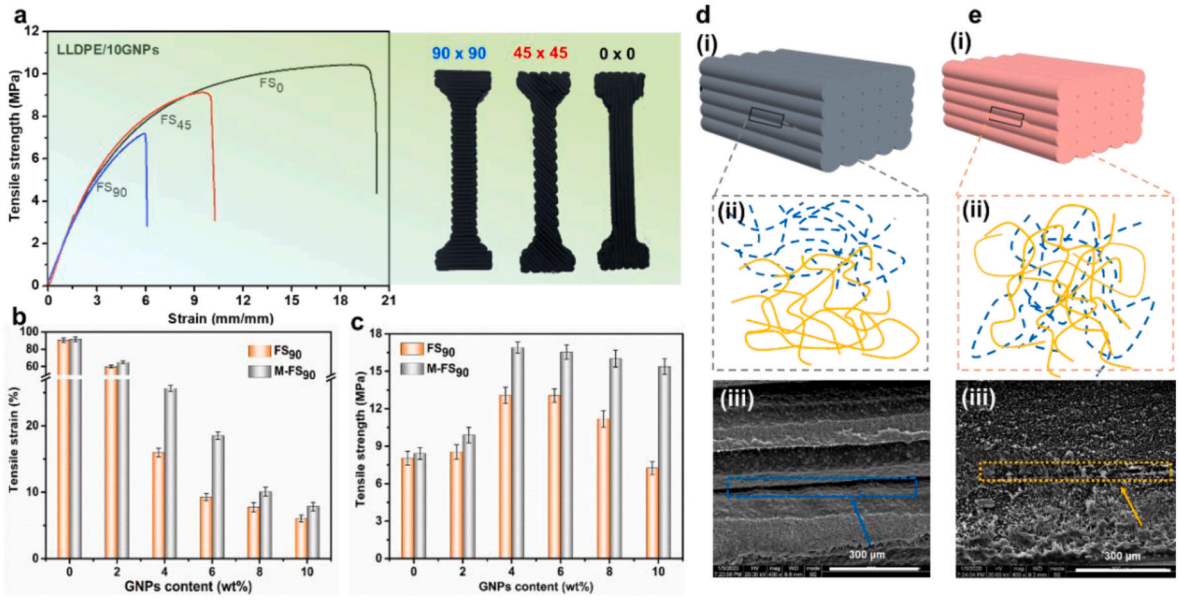

Fig. 4. Mechanical properties of LLDPE/GNPs nanocomposite parts prepared for tensile test. Stress-strain curves of LLDPE/10 GNPs parts for different printing pattern (FS_0, FS_{45} and FS_{90}) (a); mechanical property comparison between FS_{90} and M-FS_{90} parts: tensile strain (b) and tensile strength (c); Schematic for enhanced mechanism of mechanical properties before (d-ii) and after (e-ii) MW irradiation and SEM images of the stretched fractured surfaces of LLLDPE/10 GNPs parts before (d-iii) and after (e-iii) MW irradiation.

that the FDM printing of LLDPE nanocomposites can achieve a high level of accuracy.

3.3. Mechanical properties of FDM 3D printed LLDPE/GNPs parts

The tensile properties of the FDM 3D printed LLDPE/GNPs parts with different loading of GNPs and filling patterns (0 × 0, 45 × 45 and 90 × 90) are compared in Fig. 4. Fig. 4a compares the stress-strain curves of LLDPE/10 GNPs parts for different filling patterns. It is clearly seen that the FS_0 parts show the highest ultimate tensile strength of 10.5 MPa and elongation at break of 20.26%, which are nearly 1.5 and 3 times as much as that of FS_{90} (with 7.14 MPa in strength and 6.13% in strain), respectively. This is because in FS_{90} pattern, the bonding interfaces between filaments in the same deposition layer is perpendicular to the stress direction, thus making the bonding interfaces be the weakness of the whole structure. The tensile property of FS_{90} sample is therefore much lower, as also reported in the previous publications [38,49]. For this reason, the 90 × 90 printing pattern is selected to evaluate the interfacial bonding strength of FDM 3D printed parts here. To enhance the interfacial strength, MW irradiation was applied to treat the LLDPE/GNPs nanocomposite parts so as to increase their interlaminar bonding strength. The mechanical property results of FS_{90} and M-FS_{90} samples with various loading of GNPs are compared in Fig. 4b and c. As can be seen, with increasing GNPs loading, the tensile strength first increases and then decreases, while the elongation at break continuously decreases. More importantly, it is found that MW treatment equivalently enhances the tensile strength and the elongation at break of all the 3D printed parts. For tensile strength, the higher GNPs loading produces the greater enhancement, but for elongation at break, the optimum increase degree occurs in the range of 4–6 wt%. For instance, M-LLDPE/10 GNPs shows a remarkably enhanced tensile strength of 15.5 MPa, which is more than twice as high as that of untreated LLDPE/10 GNPs at 7.14 MPa. However, pure LLDPE and LLDPE/2 GNPs after microwave irradiation show only slight increase. Similarly, the elongation at break of M-LLDPE/6 GNPs reaches the optimum value of ~20%, which is about two times as high as that of LLDPE/6 GNPs at 10%. The above results show that the microwave irradiation post-treatment could effectively enhance the interfacial bonding strength of LLDPE/GNPs 3D printed parts, especially in the GNPs loading range of 4–10 wt%. The above enhancement can be explained by the selective absorption of microwaves by the GNPs fillers. Obviously, the higher loading of the homogeneously dispersed GNPs fillers in LLDPE matrix would facilitate more MW absorption and result in higher temperature, thus more efficiently heating the parts. This effect can significantly improve the interfacial bonding and hence produces a dramatic enhancement in interfacial strength, and therefore tensile property. However, for the parts with low GNPs loading (0–2 wt%), the incorporated GNPs would have the much less microwave absorption and hence result in low temperature. Consequently, the improvement in mechanical performance is very limited. The above analyses have been verified by a schematic of polymer chain diffusion and SEM morphological characterization of LLDPE/10 GNPs 3D-printed parts before and after microwave treatment (Fig. 4d and e). When a microwave field is applied, the GNPs in the filaments would absorb much of the MW energy, which would be then transformed into heat energy. Accordingly, the LLDPE matrix around the GNPs particles at the interface would be heated to promote polymer mobility and entanglement across the interface, and at the same time, the bonding area would be also increased (Fig. 4d–ii and 4e-ii). As a result, the interfacial bonding of the 3D printed parts is substantially enhanced, as presented in SEM images (Fig. 4d–iii versus Fig. 4e–iii). The effect of formation of the interconnected structures inside the printing filaments on the interfacial bonding and the further enhancement efficiency for interfacial strength was discussed in Supplementary Information (Fig. S6).

3.4. EMI shielding performances of FDM 3D printed LLDPE/GNPs parts

EMI shielding measurements of the LLDPE/GNPs nanocomposites parts were performed in the X-band (8.2–12.4 GHz), which is the frequency range widely used in telecommunication applications. To investigate the effect of MW post-manufacture treatment on the total EMI SE of the LLDPE/GNPs printed parts, the EMI SE_T of the printed parts with different GNP loading before and after MW irradiation was compared and the results are shown in Fig. S7 (Supplementary Information). As can be seen, the MW treatment shows a complicated influence on EMI SE at various GNPs loading. However, totally speaking, at high GNPs loading (>4 wt%), the effect of MW treatment on EMI shielding performance (including the microwave absorption shielding) would become very small. Additionally, the previous results show that the microwave treatment can significantly enhance the mechanical performances of LLDPE/GNPs printed parts with higher loading of GNPs. The influence of GNPs loading on the EMI SE of the LLDPE/GNPs printed parts is shown Fig. S8 (Supplementary Information). The related detailed discussion and analyses are also included in Supplementary Information. It can be accordingly concluded that only 6.0 wt% GNPs loading can impart the printed parts the EMI SE value of about 20.3 dB, which already achieves the minimum level (20 dB) required for the general commercial applications [23]. Furthermore, it is worth noting that by increasing GNPs loading to 10.0 wt%, the printed parts show an excellent averaged EMI SE of 32.4 dB at only 2 mm thickness.

To evaluate the effect of filling pattern on the EMI SE_T of the LLDPE/10 GNPs printed parts, three different filling patterns were designed for printing (0 × 0, 0 × 60 and −60 × 0 × 60). The digital photos of the corresponding mentioned 3 printed parts are clearly presented by SEM (Fig. 5a–ii, b-ii and c-ii) and super-depth-of-field images (Fig. 5a–iii, b-iii and c-iii). Fig. 5a–ii, b-ii and c-ii show the low-magnification SEM morphology of the fractured surface of $LG_{1\text{-}60}$, $LG_{2\text{-}60}$ and $LG_{3\text{-}60}$ parts, respectively. The deposition filaments with porous structures ($LG_{3\text{-}60}$) can be clearly observed from the cross-section SEM images and super-depth-of-field images in Fig. 5c. After MW treatment, the filaments are relatively more closely bonded, resulting in excellent interfacial strength. Fig. 5d shows the total EMI SE of the LLDPE/10 GNPs printed parts with the mentioned three filling patterns at 60% and 100% infill density, respectively. As can be seen, when the infill density is 100%, the EMI SE of all samples is approximately in the range of 30–32 dB and the filling pattern shows small effect on EMI SE ($LG_{3\text{-}100}$ is the optimum). However, when the infill density decreases to 60%, the different filling patterns present a significant difference in EMI SE, e.g., at 10 GHz, the $LG_{3\text{-}60}$ part possesses the optimum EMI SE of 32.4 dB, and however $LG_{1\text{-}60}$ part has the lowest one (23.8 dB). Overall, the EMI SE of infill density of 100% is higher than that of 60%, and the difference among different patterns following the order: filling pattern LG_3>LG_2>LG_1. For in-depth understanding of such difference, the SE_T, SE_A, and SE_R of the LLDPE/10 GNPs parts obtained with different filling pattern and infill density at the frequency of 10 GHz are further compared in Fig. 5e. As can be seen, both SE_R and SE_A basically contribute to SE_T, and SE_R varies little under different conditions. The difference comes chiefly from SE_A, i.e. absorption. Obviously, SE_A of LG_3 series is the largest. The influence of infill density on the total EMI SE_T of LG_3 printed parts (LLDPE/10 GNPs) in the X-band frequency range is demonstrated in Fig. 5f. As can be seen, overall, the averaged EMI SE of various sample decreases from 32.4 to 29 dB as following: $LG_{3\text{-}100}$>$LG_{3\text{-}80}$>$LG_{3\text{-}60}$>$LG_{3\text{-}40}$, i.e., the highest infill density would lead to the highest SE. However, it should be noted that the EMI SE values for infill density in the range of 60–100% are actually close and that of 40% is lower to some extent. Because high infill density means high weight, the fabrication of the heaviest parts with similar EMI SE is not cost-effective. Therefore, the 3D printed parts with low infill density and lightweight porous structure seems to be more favorable, so a thickness normalized specific SE value of SSE/t (SE divided by the sample density and thickness) [23] was used to further evaluate the EMI SE performance of LLDPE/10 GNPs parts (Fig. 5g).

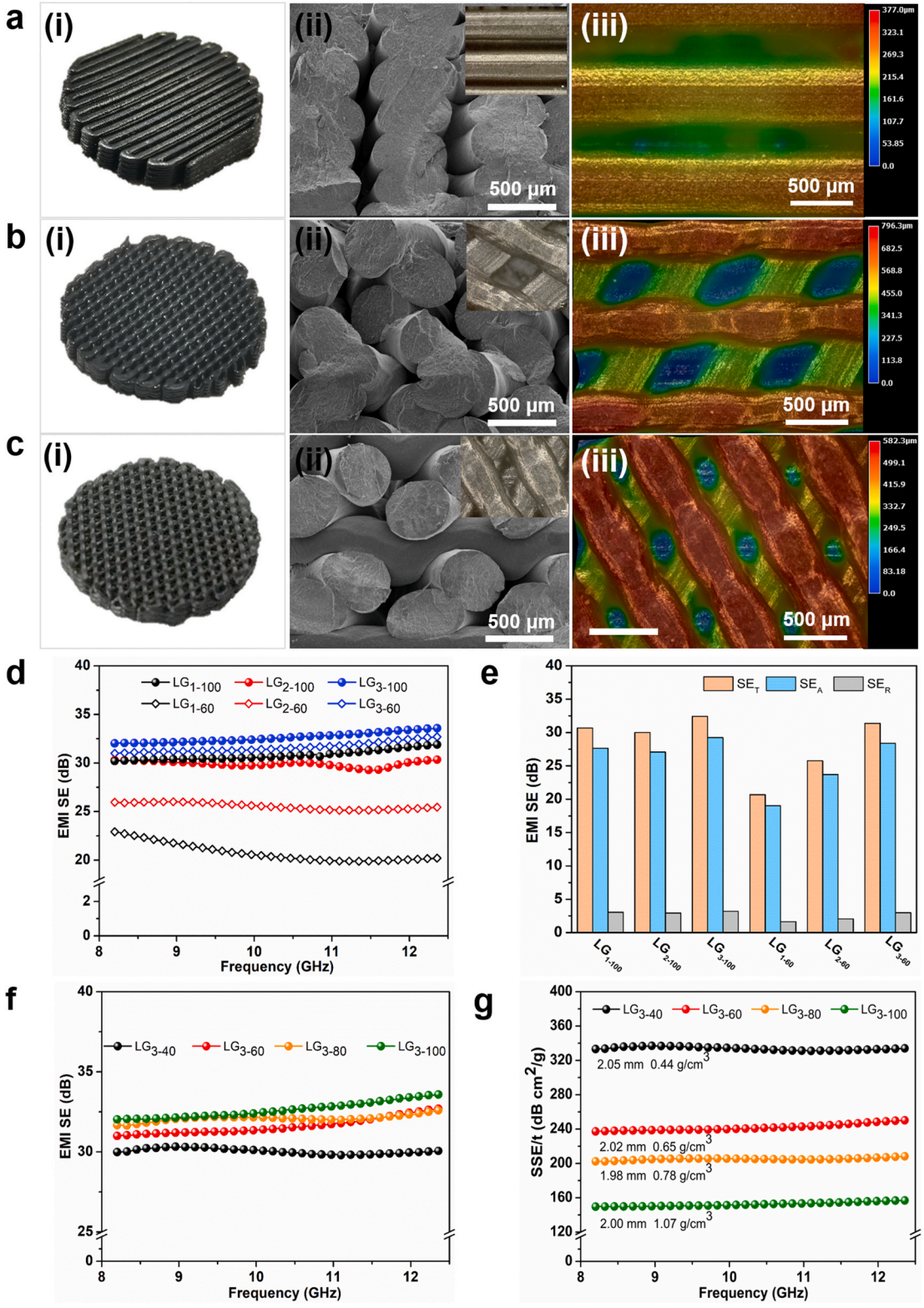

Fig. 5. Effect of the printed porous structure on EMI SE properties of LLDPE/10 GNPs parts: digital photos of $LG_{1\text{-}60}$ (a–i), $LG_{2\text{-}60}$ (b–i) and $LG_{3\text{-}60}$ (c–i) FDM printed parts, SEM images of the corresponding fractured surfaces (a-ii, b-ii and c-ii), super-depth-of-field images of filament alignments (iii), EMI SE_T of the LLDPE/GNPs parts with different filling pattern (1–3) and different infill density (60% and 100%) (d), EMI SE_T, SE_A and SE_R dependence of filling pattern and infill density at the frequency of 10 GHz (e), effect of infill density on EMI SE_T of the LLDPE/GNPs parts (f), and effect of infill density on the SSE/t of the LLDPE/GNPs parts in X-band frequency (g).

Obviously, there is a significant difference between different infill densities. The printed part with lower infill density clearly shows a much higher SSE/t. For instance, by decreasing the infill density from 100% to 40%, the average SSE/t of printed parts increases remarkably from 152 to 318 dB cm^2/g. As a result, the lightweight porous LLDPE/10 GNPs parts printed with filling pattern 3 and infill density of 40% actually possesses the optimum SSE/t while having a transmission shielding effectiveness around 30 dB. Furthermore, a detailed comparison in EMI SE between our 3D printed porous parts and other lightweight EMI shields reported in literatures [20,23,25,50–54] was shown in Fig. 6. Comparatively, the specific FDM 3D-printed parts prepared by our strategy exhibit a relatively higher EMI SE at a lower density, indicating that the FDM-printed porous lamellar structure presents a certain advantage over some other technologies reported in above mentioned literatures.

Based on the structure of the LLDPE/GNPs printed porous part, a possible EMI shielding mechanism is presented in Fig. 7a. When the incident EM waves are applied to the printed part surface, a small fraction of the EM waves are reflected back. The remaining EM waves are transmitted inside and further interact with the porous structures of the printed parts, leading to energy loss of the EM waves. As well known, the better impedance match could result in the more absorption of EM waves [55] because the impedance match between porous material and free space is better than that of solid materials [56]. In order to better illustrate the electromagnetic interference shielding mechanism, the test of dielectric parameters of the printed porous parts have been carried out. The results are exhibited in Fig. S9. As shown in Fig. S9, the LG_3 series present the relative higher imaginary permittivity ε'' than other patterns. This demonstrates that the alternating internal interface of LG_3 series facilitates multiple reflections and absorption of incidence EM wave, and results in more electric energy loss [37,57], as exhibited in the enlarged picture (Fig. 7a–iii). The above analyses and discussions could illustrate the higher EMI shielding effectiveness of the FDM 3D printed porous parts due to the more absorption of EM waves and the enhanced internal electric energy loss. Of course, this explanation needs further confirmation by computer simulation of the EM wave propagation inside the structure, which will be further investigated in detail later. Herein, it should be stressed again that the lower infill density can simultaneously achieve an enhancement in the specific EMI SE and reduction in density. The 3D printed LLDPE/GNPs part with infill density of 40% possesses an attracting low density (only 0.44 g/cm^3) and the highest SSE/t value, showing a very promising application prospect. The various types of complex porous parts can be printed under the similar conditions, which are presented in Fig. 7b. Obviously, this is a facile strategy which could be highly proposed to fabricate the lightweight and multifunctional parts through the FDM 3D printing technology.

4. Conclusions

In conclusion, lamellar porous and lightweight LLDPE/GNPs nanocomposite structures with enhanced interfacial bonding strength and the excellent EMI SE were successfully prepared through a combination of FDM 3D printing, ball milling and microwave irradiation strategies. The LLDPE/GNPs printed parts show a remarkable EMI SE of 32.4 dB at 10 GHz. The ball milling technology was used to realize exfoliation and dispersion of GNPs in the polymer matrix, which is advantageous for the construction of a segregated conductive network and microwave absorption. The FDM 3D printing strategy could enable us to tailor the EMI SE of the LLDPE/GNPs printed parts by adjusting the printing parameters, and realize the fabrication of lightweight and layered porous 3D printed parts with complex shape/structure. The results obtained in the present work show that the specific EMI SE (SSE/t) of the LLDPE/GNPs printed parts is dramatically improved with decreasing the infill density from 100% to 40%. In addition, microwave irradiation technology significantly enhances the interfacial bonding between filaments of the 3D printed parts with higher GNPs loading (4–10 wt%), thus resulting in a remarkable increase in both tensile strength and elongation at break. Under the optimized preparation conditions, the fabricated LLDPE/GNPs 3D printed porous parts possess excellent EMI shielding effectiveness with SSE/t equal to 318 dB cm^2/g, significantly enhanced mechanical robustness with 13.63 MPa tensile strength and lightweight feature (density of only 0.44 g/cm^3). By an innovative combination of the above approaches, high-performance EMI shielding parts with various complex geometry and structure can be fabricated. The current study provides a promising facile strategy for fabricating high-

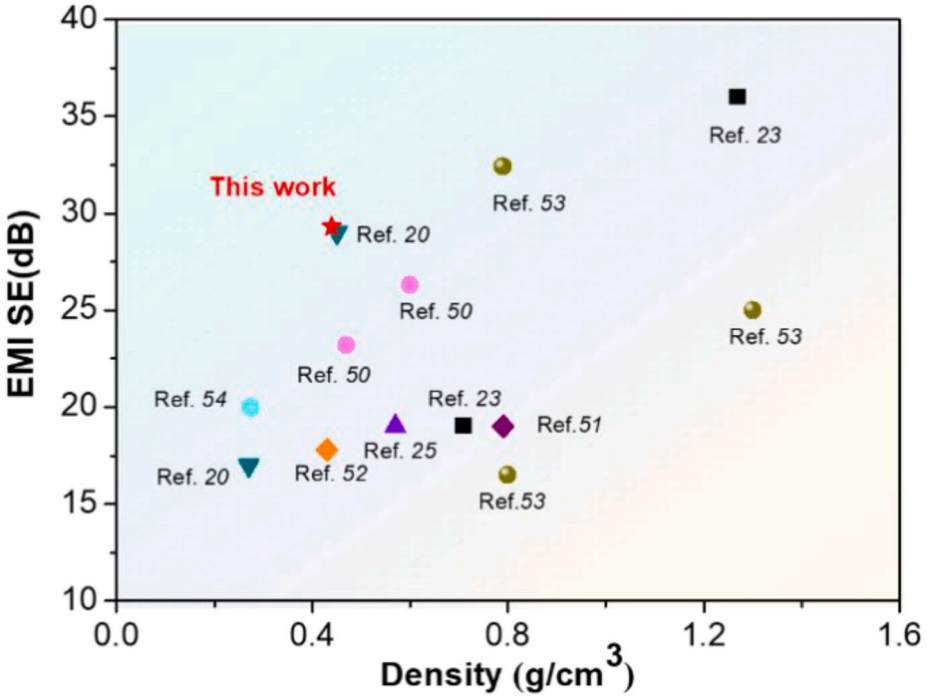

Fig. 6. Comparison in EMI SE between our work and other lightweight EMI shields in literatures.

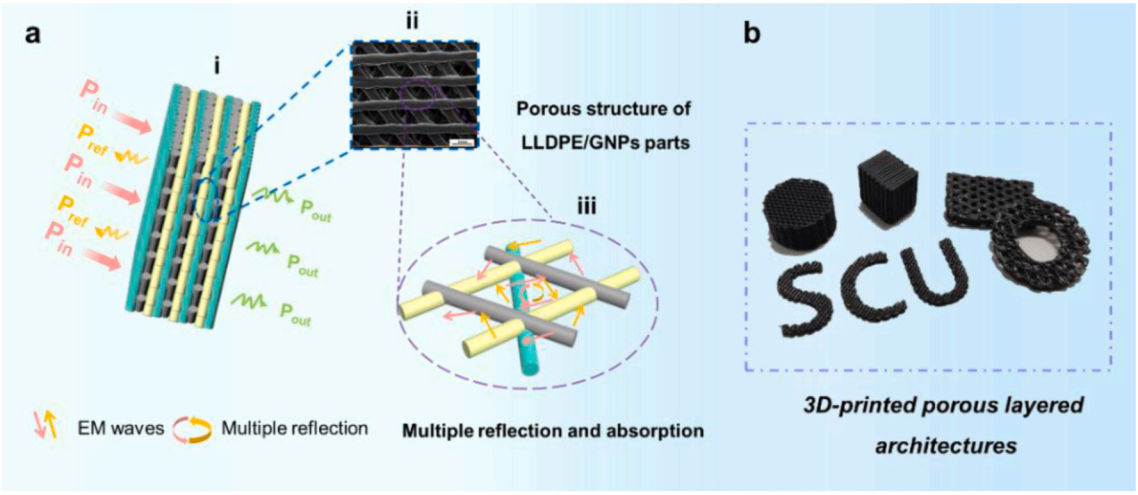

Fig. 7. Schematic diagram for illustrating the EMI shielding mechanism of LLDPE/GNPs printed part (a), and digital photo of the printed porous layered architectures (b).

performance EMI shielding 3D printed parts to be potentially applied in aerospace facilities and lightweight portable electronic devices. Even higher EMI shielding performance of 3D printed parts can be expected by optimizing more complex 3D printing structures and filling patterns.

Declaration of competing interest

The authors declare that they have no known competing financial interests or personal relationships that could have appeared to influence the work reported in this paper.

Acknowledgments

This work is financially supported by the National Key R&D Program of China (2017YFE0111500), the National Natural Science Foundation of China (51933007 and 51721091), the International Science & Technology Innovation Cooperation Project of Sichuan Province (2021YFH0088), the European Union's H2020-MSCA-RISE-734164 Graphene 3D Project, the Project of State Key Laboratory of Polymer Materials Engineering (Sichuan University) (sklpme2020-2-01), and the Program of Innovative Research Team for Young Scientists of Sichuan Province (2016TD0010).

Appendix A. Supplementary data

Supplementary data to this article can be found online at https://doi.org/10.1016/j.compscitech.2021.108732.

CRediT authorship contribution statement

Jingjing Jing: Writing - original draft, Data curation, Formal analysis, Conceptualization. **Yu Xiong:** Data curation, Validation. **Shaohong Shi:** Conceptualization, Methodology, Investigation. **Haoran Pei:** Investigation, Validation, Formal analysis. **Yinghong Chen:** Funding acquisition, Resources, Writing - review & editing, Supervision. **Philippe Lambin:** Review & editing, Supervision.

References

[1] W.T. Cao, F.F. Chen, Y.J. Zhu, Y.G. Zhang, Y.Y. Jiang, M.G. Ma, F. Chen, Binary strengthening and toughening of MXene/cellulose nanofiber composite paper with nacre-inspired structure and superior electromagnetic interference shielding properties, ACS Nano 12 (2018) 4583–4593.

[2] W.-C. Yu, G.-Q. Zhang, Y.-H. Liu, L. Xu, D.-X. Yan, H.-D. Huang, J.-H. Tang, J.-Z. Xu, Z.-M. Li, Selective electromagnetic interference shielding performance and superior mechanical strength of conductive polymer composites with oriented segregated conductive networks, Chem. Eng. J. 373 (2019) 556–564.

[3] C.-F. Cao, G.-D. Zhang, L. Zhao, L.-X. Gong, J.-F. Gao, J.-X. Jiang, L.-C. Tang, Y.-W. Mai, Design of mechanically stable, electrically conductive and highly hydrophobic three-dimensional graphene nanoribbon composites by modulating the interconnected network on polymer foam skeleton, Compos. Sci. Technol. 171 (2019) 162–170.

[4] F. Kargar, Z. Barani, M. Balinskiy, A.S. Magana, J.S. Lewis, A.A. Balandin, Dual-functional graphene composites for electromagnetic shielding and thermal management, Adv. Electron. Mater. 5 (2019) 1800558.

[5] S.T. Hsiao, C.C. Ma, W.H. Liao, Y.S. Wang, S.M. Li, Y.C. Huang, R.B. Yang, W. F. Liang, Lightweight and flexible reduced graphene oxide/water-borne polyurethane composites with high electrical conductivity and excellent electromagnetic interference shielding performance, ACS Appl. Mater. Interfaces 6 (2014) 10667–10678.

[6] M.-S. Cao, W.-L. Song, Z.-L. Hou, B. Wen, J. Yuan, The effects of temperature and frequency on the dielectric properties, electromagnetic interference shielding and microwave-absorption of short carbon fiber/silica composites, Carbon 48 (2010) 788–796.

[7] Y. Wang, Y. Du, R. Qiang, C. Tian, P. Xu, X. Han, Interfacially engineered sandwich-like rGO/carbon microspheres/rGO composite as an efficient and durable microwave absorber, Adv. Mater. Interfaces 3 (2016) 1500684.

[8] X. Zhang, J. Zhang, L. Xia, J. Wang, C. Li, F. Xu, X. Zhang, H. Wu, S. Guo, Achieving high-efficiency and robust 3D thermally conductive while electrically insulating hybrid filler network with high orientation and ordered distribution, Chem. Eng. J. 334 (2018) 247–256.

[9] W. Wang, R. Li, M. Tian, L. Liu, H. Zou, X. Zhao, L. Zhang, Surface silverized meta-aramid fibers prepared by bio-inspired poly(dopamine) functionalization, Adv. Mater. Interfaces 5 (2013) 2062–2069.

[10] Y. Wang, L.-j. Ni, F. Yang, F.-q. Gu, K. Liang, K. Marcus, Y.-d. Wan, J.-j. Chen, Z.-s. Feng, Facile preparation of a high-quality copper layer on epoxy resin via electroless plating for applications in electromagnetic interference shielding, J. Mater. Chem. C 5 (2017) 12769–12776.

[11] K. Zhang, Y. Li, H. Zhou, M. Nie, Q. Wang, Z. Hua, Polyurethane/carbon fiber composite tubular electrode featuring three-dimensional interpenetrating conductive network, Carbon 139 (2018) 999–1009.

[12] J. Ling, W. Zhai, W. Feng, B. Shen, J. Zhang, W. Zheng, Facile preparation of lightweight microcellular polyetherimide/graphene composite foams for electromagnetic interference shielding, ACS Appl. Mater. Interfaces 5 (2013) 2677–2684.

[13] L.-C. Jia, G. Zhang, L. Xu, W.-J. Sun, G.-J. Zhong, J. Lei, D.-X. Yan, Z.-M. Li, Robustly superhydrophobic conductive textile for efficient electromagnetic interference shielding, ACS Appl. Mater. Interfaces 11 (2018) 1680–1688.

[14] Y.J. Wan, P.L. Zhu, S.H. Yu, R. Sun, C.P. Wong, W.H. Liao, Anticorrosive, ultralight, and flexible carbon-wrapped metallic nanowire hybrid sponges for highly efficient electromagnetic interference shielding, Small 14 (2018), e1800534.

[15] C. Li, C. Zhou, J. Lv, B. Liang, R. Li, Y. Liu, J. Hu, K. Zeng, G. Yang, Bio-molecule adenine building block effectively enhances electromagnetic interference shielding performance of polyimide-derived carbon foam, Carbon 149 (2019) 190–202.

[16] M. Kim, J.H. Jeong, J.Y. Lee, A. Capasso, F. Bonaccorso, S.H. Kang, Y.K. Lee, G. H. Lee, Electrically conducting and mechanically strong graphene-polylactic acid composites for 3D printing, ACS Appl. Mater. Interfaces 11 (2019) 11841–11848.

[17] A. Ameli, M. Nofar, S. Wang, C.B. Park, Lightweight polypropylene/stainless-steel fiber composite foams with low percolation for efficient electromagnetic interference shielding, ACS Appl. Mater. Interfaces 6 (2014) 11091–11100.

[18] Y. Tang, S. Gong, Y. Chen, L.W. Yap, W. Cheng, Manufacturable conducting rubber ambers and stretchable conductors from copper nanowire aerogel monoliths, ACS Nano 8 (2014) 5707–5714.
[19] S. Deville, E. Saiz, R.K. Nalla, A.P. Tomsia, Freezing as a path to build complex composites, Science 311 (2006) 515–518.
[20] D.-X. Yan, P.-G. Ren, H. Pang, Q. Fu, M.-B. Yang, Z.-M. Li, Efficient electromagnetic interference shielding of lightweight graphene/polystyrene composite, J. Mater. Chem. 22 (2012) 18772.
[21] D. Feng, Q. Wang, D. Xu, P. Liu, Microwave assisted sinter molding of polyetherimide/carbon nanotubes composites with segregated structure for high-performance EMI shielding applications, Compos. Sci. Technol. 182 (2019) 107753.
[22] D. Feng, D. Xu, Q. Wang, P. Liu, Highly stretchable electromagnetic interference (EMI) shielding segregated polyurethane/carbon nanotube composites fabricated by microwave selective sintering, J. Mater. Chem. C 7 (2019) 7938–7946.
[23] D. Feng, P. Liu, Q. Wang, Exploiting the piezoresistivity and EMI shielding of polyetherimide/carbon nanotube foams by tailoring their porous morphology and segregated CNT networks, Composites, Part A 124 (2019) 105463.
[24] C. Liang, H. Qiu, Y. Han, H. Gu, P. Song, L. Wang, J. Kong, D. Cao, J. Gu, Superior electromagnetic interference shielding 3D graphene nanoplatelets/reduced graphene oxide foam/epoxy nanocomposites with high thermal conductivity, J. Mater. Chem. C 7 (2019) 2725–2733.
[25] H.B. Zhang, Q. Yan, W.G. Zheng, Z. He, Z.Z. Yu, Tough graphene-polymer microcellular foams for electromagnetic interference shielding, ACS Appl. Mater. Interfaces 3 (2011) 918–924.
[26] S. Waheed, J.M. Cabot, P. Smejkal, S. Farajikhah, S. Sayyar, P.C. Innis, S. Beirne, G. Barnsley, T.W. Lewis, M.C. Breadmore, B. Paull, Three-dimensional printing of abrasive, hard, and thermally conductive synthetic microdiamond-polymer composite using low-cost fused deposition modeling printer, ACS Appl. Mater. Interfaces 11 (2019) 4353–4363.
[27] Q. Chen, J.D. Mangadlao, J. Wallat, A. De Leon, J.K. Pokorski, R.C. Advincula, 3D printing biocompatible polyurethane/poly(lactic acid)/graphene oxide nanocomposites: anisotropic properties, ACS Appl. Mater. Interfaces 9 (2017) 4015–4023.
[28] K. Chizari, M. Arjmand, Z. Liu, U. Sundararaj, D. Therriault, Three-dimensional printing of highly conductive polymer nanocomposites for EMI shielding applications, Mater. Today Commun. 11 (2017) 112–118.
[29] L. Wang, M. Neumann, T. Fu, W. Li, X. Cheng, B.-L. Su, Porous and responsive hydrogels for cell therapy, Curr. Opin. Colloid Interface Sci. 38 (2018) 135–157.
[30] G. Chen, N. Chen, Q. Wang, Fabrication and properties of poly(vinyl alcohol)/β-tricalcium phosphate composite scaffolds via fused deposition modeling for bone tissue engineering, Compos. Sci. Technol. 172 (2019) 17–28.
[31] S.E. Lowe, G. Shi, Y. Zhang, J. Qin, S. Wang, A. Uijtendaal, J. Sun, L. Jiang, S. Jiang, D. Qi, M. Al-Mamun, P. Liu, Y.L. Zhong, H. Zhao, Scalable production of graphene oxide using a 3D-printed packed-bed electrochemical reactor with a boron-doped diamond electrode, ACS Appl. Nano Mater. 2 (2019) 867–878.
[32] J.H. Kim, W.S. Chang, D. Kim, J.R. Yang, J.T. Han, G.W. Lee, J.T. Kim, S.K. Seol, 3D printing of reduced graphene oxide nanowires, Adv. Mater. 27 (2015) 157–161.
[33] S. Gantenbein, K. Masania, W. Woigk, J.P.W. Sesseg, T.A. Tervoort, A.R. Studart, Three-dimensional printing of hierarchical liquid-crystal-polymer structures, Nature 561 (2018) 226–230.
[34] L. Yang, Y. Chen, M. Wang, S. Shi, J. Jing, Fused deposition modeling 3D printing of novel poly(vinyl alcohol)/graphene nanocomposite with enhanced mechanical and electromagnetic interference shielding properties, Ind. Eng. Chem. Res. 59 (2020) 8066–8077.
[35] L. Ecco, S. Dul, D. Schmitz, G. Barra, B. Soares, L. Fambri, A. Pegoretti, Rapid prototyping of efficient electromagnetic interference shielding polymer composites via fused deposition modeling, Appl. Sci. 9 (2018) 37.
[36] D.P. Schmitz, L.G. Ecco, S. Dul, E.C.L. Pereira, B.G. Soares, G.M.O. Barra, A. Pegoretti, Electromagnetic interference shielding effectiveness of ABS carbon-based composites manufactured via fused deposition modelling, Mater. Today Commun. 15 (2018) 70–80.
[37] X. Li, X. Yin, H. Xu, M. Han, M. Li, S. Liang, L. Cheng, L. Zhang, Ultralight MXene-coated, interconnected SiCnws three-dimensional lamellar foams for efficient microwave absorption in the X-band, ACS Appl. Mater. Interfaces 10 (2018) 34524–34533.
[38] J. Wang, H. Xie, Z. Weng, T. Senthil, L. Wu, A novel approach to improve mechanical properties of parts fabricated by fused deposition modeling, Mater. Des. 105 (2016) 152–159.
[39] L. Yang, S. Li, X. Zhou, J. Liu, Y. Li, M. Yang, Q. Yuan, W. Zhang, Effects of carbon nanotube on the thermal, mechanical, and electrical properties of PLA/CNT printed parts in the FDM process, Synth. Met. 253 (2019) 122–130.
[40] S. Tarafder, V.K. Balla, N.M. Davies, A. Bandyopadhyay, S. Bose, Microwave-sintered 3D printed tricalcium phosphate scaffolds for bone tissue engineering, J. Tissue Eng. Regener. Med. 7 (2013) 631–641.
[41] T.J. Imholt, C.A. Dyke, B. Hasslacher, J.M. Perez, D.W. Price, J.A. Roberts, J. B. Scott, A. Wadhawan, Z.Y.M. Tour, Nanotubes in microwave fields: light emission, intense heat, outgassing, and reconstruction, Chem. Mater. 15 (2003) 3969–3970.
[42] D.-X. Yan, H. Pang, B. Li, R. Vajtai, L. Xu, P.-G. Ren, J.-H. Wang, Z.-M. Li, Structured reduced graphene oxide/polymer composites for ultra-efficient electromagnetic interference shielding, Adv. Funct. Mater. 25 (2015) 559–566.
[43] J.B. Wu, M.L. Lin, X. Cong, H.N. Liu, P.H. Tan, Raman spectroscopy of graphene-based materials and its applications in related devices, Chem. Soc. Rev. 47 (2018) 1822–1873.
[44] J. Jing, Y. Chen, S. Shi, L. Yang, P. Lambin, Facile and scalable fabrication of highly thermal conductive polyethylene/graphene nanocomposites by combining solid-state shear milling and FDM 3D-printing aligning methods, Chem. Eng. J. 402 (2020) 126218.
[45] S. Shi, Z. Peng, J. Jing, L. Yang, Y. Chen, 3D printing of delicately controllable cellular nanocomposites based on polylactic acid incorporating graphene/carbon nanotube hybrids for efficient electromagnetic interference shielding, ACS Sustain. Chem. Eng. 8 (2020) 7962–7972.
[46] S. Yang, S. Bai, W. Duan, Q. Wang, Production of value-added composites from aluminum–plastic package waste via solid-state shear milling process, ACS Sustain. Chem. Eng. 6 (2018) 4282–4293.
[47] B. Li, W.-H. Zhong, Review on polymer/graphite nanoplatelet nanocomposites, J. Mater. Sci. 46 (2011) 5595–5614.
[48] F. Du, R.C. Scogna, W. Zhou, S. Brand, J.E. Fischer, K.I. Winey, Nanotube networks in polymer nanocomposites: rheology and electrical conductivity, Macromolecules 37 9048-9055.
[49] K.I. Byberg, A.W. Gebisa, H.G. Lemu, Mechanical properties of ULTEM 9085 material processed by fused deposition modeling, Polym. Test. 72 (2018) 335–347.
[50] J. Chen, X. Liao, W. Xiao, J. Yang, Q. Jiang, G. Li, Facile and green method to structure ultralow-threshold and lightweight polystyrene/MWCNT composites with segregated conductive networks for efficient electromagnetic interference shielding, ACS Sustain. Chem. Eng. 7 (2019) 9904–9915.
[51] M.C.G. Yonglai Yang, Novel carbon Nanotube−Polystyrene foam composites for electromagnetic interference shielding, Nano letter 5 (2005) 2131–2134.
[52] B. Shen, W. Zhai, M. Tao, J. Ling, W. Zheng, Lightweight, multifunctional polyetherimide/graphene@Fe_3O_4 composite foams for shielding of electromagnetic pollution, ACS Appl. Mater. Interfaces 5 (2013) 11383–11391.
[53] H. Wang, K. Zheng, X. Zhang, X. Ding, Z. Zhang, C. Bao, L. Guo, L. Chen, X. Tian, 3D network porous polymeric composites with outstanding electromagnetic interference shielding, Compos. Sci. Technol. 125 (2016) 22–29.
[54] J. Ju, T. Kuang, X. Ke, M. Zeng, Z. Chen, S. Zhang, X. Peng, Lightweight multifunctional polypropylene/carbon nanotubes/carbon black nanocomposite foams with segregated structure, ultralow percolation threshold and enhanced electromagnetic interference shielding performance, Compos. Sci. Technol. 193 (2020) 108116.
[55] H. Lv, X. Liang, G. Ji, H. Zhang, Y. Du, Porous three-dimensional flower-like Co/CoO and its excellent electromagnetic absorption properties, ACS Appl. Mater. Interfaces 7 (2015) 9776–9783.
[56] H. Mei, X. Zhao, S. Zhou, D. Han, S. Xiao, L. Cheng, 3D-printed oblique honeycomb Al2O3/SiCw structure for electromagnetic wave absorption, Chem. Eng. J. 372 (2019) 940–945.
[57] H. Xu, X. Yin, X. Li, M. Li, S. Liang, L. Zhang, L. Cheng, Lightweight Ti2CT x MXene/poly(vinyl alcohol) composite foams for electromagnetic wave shielding with absorption-dominated feature, ACS Appl. Mater. Interfaces 11 (2019) 10198–10207.